Using the Transient IR Spectroscopy to Elucidate Reaction Mechanisms in Visible Light Photoredox Catalysis:

Author: Jingchen Yang

Persistent link: http://hdl.handle.net/2345/bc-ir:108934

This work is posted on eScholarship@BC,
Boston College University Libraries.

Boston College Electronic Thesis or Dissertation, 2020

Copyright is held by the author, with all rights reserved, unless otherwise noted.

Using the Transient IR Spectroscopy to Elucidate Reaction Mechanisms in Visible Light Photoredox Catalysis

Jingchen Yang

A thesis
submitted to the Faculty of
the department of Chemistry
in partial fulfillment
of the requirements for the degree of
Master of Science

Boston College
Morrissey College of Arts and Sciences
Graduate School

August 2020

Copyright © 2020 by Jingchen Yang

Using the Transient IR Spectroscopy to Elucidate Reaction Mechanisms in Visible Light Photoredox Catalysis

Jingchen Yang
Advisors: Matthias Waegele, Assistant Professor of Chemistry
Committee Members: Dunwei Wang, Professor of Chemistry
Chia-Kuang Tsung, Associate Professor
Udayan Mohanty, Professor of Chemistry

Studying the visible light-driven photoredox catalysis coupled with transition-metal complexes is of overriding importance in the development of synthetic strategy. Comparing to conventional thermal catalysis, reactions catalyzed and/ or initiated by photon energy are not only attractive for establishing a more sustainable system, but also for their unique reactivity that has previously been inaccessible. However, one issue draws our attention is that such photoredox catalytic schemes often suffer from a limited substrate scope. To develop more efficient and effective synthetic strategies applicable to broader range of substrates, it is of our interest to construct an functional and reliable instrument to identify the critical mechanistic steps that lead to low product yield.

To this end, we designed a time-resolved visible-pump/ infrared-probe spectroscopic measurement technique to monitor reaction dynamics in-situ. Using our transmission infrared setup, we effectively demonstrated in-situ photoexcitation and decay process of Tris(2,2-bipyridyl)dichlororuthenium(II) hexahydrate in deuterated acetonitrile. In addition, to optimize signal resolution, an electronic filter was installed in one of the data-collecting channels to allow for concurrent AC-coupled and DC-coupled signal recording. A series of chopper wheel experiments was conducted to assure the functionality of the system and reliability of obtained data.

Contents

1 Project Background and Motivation **1**

1.1 Brief Overview of Photoredox Catalysis 1

1.2 Mechanistic Questions 5

2 Methods for Probing Photoredox Catalytic Reactions **6**

2.1 Infrared Absorption Spectroscopy 6

2.2 Fourier-Transform Infrared Spectroscopy 8

2.3 Step-Scan versus Rapid-Scan FTIR 10

3 Construction of Step-Scan Pump-Probe FTIR Setup **13**

3.1 Experimental Components 13

3.1.1 Laser 14

3.1.2 FTIR Spectrometer 15

3.1.3 MCT Detector 16

3.1.4 Electronics 16

3.1.5 Flow Cell 18

3.2 Experimental Results 18

3.2.1 Pump-Probe Experiment of $Ru(bpy)_3^{2+}$ 18

3.2.2 Chopper Wheel Experiment 21

3.3 Conclusions 23

List of Figures

1.1 Simplified molecular orbital diagram of $Ru(bpy)_3^{2+}$ upon photo-excitation. Modified from [4]. 2
1.2 Proposed mechanism of photoredox reduction of electron-deficient olefins redrawn from [12]. 3
1.3 Proposed mechanism of aerobic oxidation of benzylic halides redrawn from [13]. 3
1.4 Triplet-Triplet Energy Transfer from $Ru(bpy)_3^{2+*}$ to acceptor A. Redrawn from [4]. 4

2.1 **Left**: Potential energy, E, versus internuclear distance, X, for a diatomic harmonic oscillator. **Right**: Potential energy, E, versus internuclear distance, X, for an anharmonic oscillator. Transitions originate from the v = 0 level, and D_o is the energy necessary to break the bond. D_e is the dissociation energy. Modified from [31]. 7
2.2 A scheme of Michelson interferometer. The beam splitter divides the incident beam into two beams with an optical path difference ($\boldsymbol{\delta}$) that depends on the location of the movable mirror. 9
2.3 Schematic diagram of data acquisition and data analysis in Step-Scan FTIR redrawn from [36]. The transient data are recorded as a function of time at mirror position 1, then mirror position 2, etc., and then followed up by a transpose to generate interferograms. 11

3.1 Schematic diagram of complete experimental setup. 13
3.2 Overview of Laser system. **A**: Laser Head, **B**: Controller panel, **C**: Power supply, **D**: Heat exchanger 14
3.3 General overview of Vertex 70 FTIR spectrometer (Top view). **A**: Electronics compartment, **B**: Detector compartment, **C**: Interferometer compartment, **D**: Sample compartment, **E**: Beam direction control compartment 15
3.4 The sample compartment is equipped with a QuickLock locking mechanism ① , which allows for an exact and reproducible positioning of the accessory in the sample compartment. 16
3.5 Schematic diagram of connection between detector and transient recording board. 17

3.6 Schematic design of IR flow cell. 18
3.7 UV-Vis absorption spectrum of $Ru(bpy)_3^{2+}$ together with a simplified molecular orbital diagram. 19
3.8 **Left**: Comparison of experimental ground-state spectrum of $Ru(bpy)_3^{2+}$ with Omberg *et al.* [46]. **Right**: Comparison of experimental time-resolved Infrared (TRIR) spectra of $Ru(bpy)_3^{2+}$ with Omberg *et al.* [46] 20
3.9 Optimized exponential decay fitting of $Ru(bpy)_3^{2+}$*. Fitted lifetime for phase-corrected AC-coupled signal is 0.325 ± 0.072 μs. 21
3.10 Scheme of Chopper Wheel Experiment. **A**: When infrared light passes through chopper wheel, signal is detected. **B**: When infrared light is blocked by chopper wheel, no signal is detected. 21
3.11 Initial results without phase correction. **Left**: Results of input range of $\pm$500mV. **Right**: Results of input range of $\pm$1V. 22
3.12 Results after phase correction. **Left**: Results of input range of $\pm$500mV. **Right**: Results of input range of $\pm$1V. 22

Acknowledgments

I would like to express my deepest appreciation to my advisor and labmates: Matthias Waegele, Xiang Li, Jingyi Li, Charuni Gunathunge, Vincent Ovalle, and Julie Hong.
I would like to extend my sincere thanks to Chao Liu, Wei-Shang (Victor) Lo, and Yuyang Zhang for helping me both as researchers and as my friends.
Last, I would like to extend my gratitude to my parents, who have always been supporting me in my life.

Chapter 1

Project Background and Motivation

1.1 Brief Overview of Photoredox Catalysis

Contemporarily, human activities such as industry, agriculture, and transportation have posed a series of ecological problems. Such increasing demand of conventional energy sources has caused disturbances in the ecological balance beyond its adaptive capacity [1]. On the contrary, as an energy source delivered from outer space, solar energy nowadays is considered as the ultimate sustainable energy source available to human beings [2]. In this regard, since last century [3, 4], not only in terms of solar energy conversion but also for organic synthesis, visible light-driven photoredox catalysis has gradually drawn increasing recognition as an ecofriendly yet powerful technique. During the past decade in particular, the rapid development of novel photoredox catalytic strategies has strongly demonstrated the impressive potential buried within the visible light-driven photoredox catalysis [5–7]. Thus, systematic mechanistic studies would benefit to future catalyst-design in similar photoredox catalytic conditions and therefore gain our research interests.

As an old concept, visible light-driven photoredox catalysis has experienced a tremendous revival in the past decade, leading to important progress in both organic [8] and inorganic chemistry [9]. Generally, visible light-driven photoredox catalysis relies on the ability of transition metal complexes and organic dyes to participate in energy-/electron-transfer processes with organic substrates upon photoexcitation with visible light [4]. Comparing to chemical transformations promoted by ultraviolet light, the low energies of photons in visible light (2 – 3 eV) is more relative to bond energies in organic molecules (typically $\geq$3.4 eV) [10], thus can prevent from possible photo-damage of product species [4].

Among the most commonly encountered visible light photocatalysts, many of them are polypyridyl complexes of ruthenium and iridium, which can absorb visible light to give stable, long-lived photoexcited states [11]. Specifically, as a prototypical photoredox catalyst tris(2,2-bipyridine)ruthenium(II), or $Ru(bpy)_3^{2+}$, upon absorption of a photon in the visible region, an electron in one of its metal-centered t_{2g} orbitals is excited to a ligand-centered π^* orbital (Figure 1.1) [11]. Such transition is so-called a metal to ligand charge transfer (MLCT). Followed by a rapid intersystem crossing (ISC), the initially occupied

singlet MLCT state fast transforms to the lowest-energy triplet MLCT state, which has an extraordinary property of being both more oxidizing and more reducing than the ground-state species [4]. As a result, the redox transformations of $Ru(bpy)_3^{2+*}$ can be utilized either via oxidative or reductive quenching.

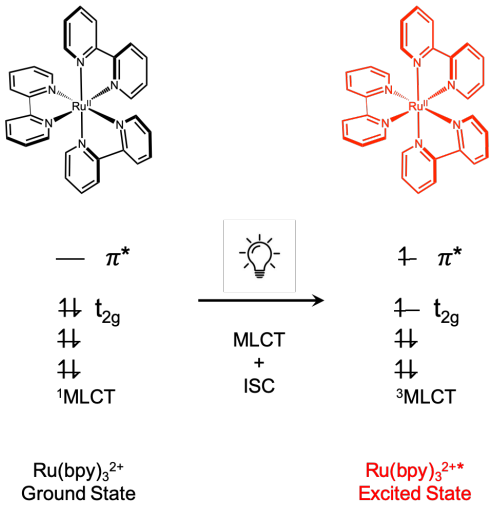

Figure 1.1: Simplified molecular orbital diagram of $Ru(bpy)_3^{2+}$ upon photo-excitation. Modified from [4].

The potential utility of $Ru(bpy)_3^{2+*}$ in organic synthesis was first demonstrated by net reductive reactions, and one of the earliest contributions was made by Pac and co-workers in 1981 describing the $Ru(bpy)_3^{2+}$-mediated reduction of electron-deficient olefins [12]. They reported that a catalyst system consisting of 2 equiv of 1-benzyl-1,4-dihydronicotinamide (BNAH, **1**) and catalytic amounts of $Ru(bpy)_3^{2+}$, upon irradiation with visible light, was able to reduce dimethyl maleate (**2**) to dimethyl succinate (**3**) via reductive quenching of $Ru(bpy)_3^{2+*}$ (Figure 1.2).

Similar to photoredox catalysis that participates in net reductive reactions in the presence of a stoichiometric electron donor, it may also contribute to net oxidative reactions along with a stoichiometric electron acceptor. In 2011, Jiao and co-workers reported a method for the photoredox oxidation of α-haloesters to α-ketoesters [13]. In their proposed mechanism, with catalytic amounts of 4-methoxypyridine (**10**) and $Ru(bpy)_3^{2+}$, ethyl -bromophenylacetate (**9**) is converted into ethyl benzoylformate (**11**) in air (Figure 1.3). In the photoredox cycle, $Ru(bpy)_3^{2+}$ readily goes to excited state $Ru(bpy)_3^{2+*}$ via MLCT by accepting a photon from visible light. Subsequently, an electron donated by the O_2^- radicals reduce the $Ru(bpy)_3^{2+*}$ to regenerate the active reductant $Ru(bpy)_3^+$ and thus close the photoredox cycle.

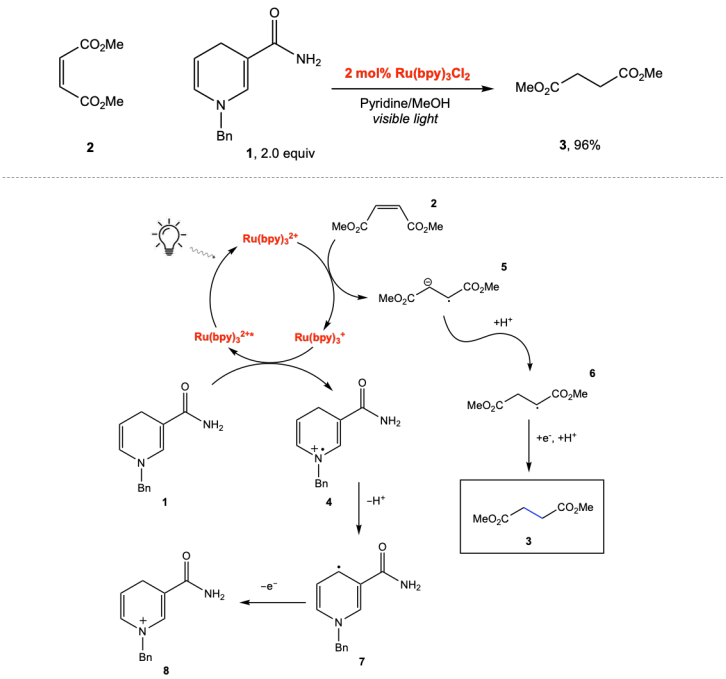

Figure 1.2: Proposed mechanism of photoredox reduction of electron-deficient olefins redrawn from [12].

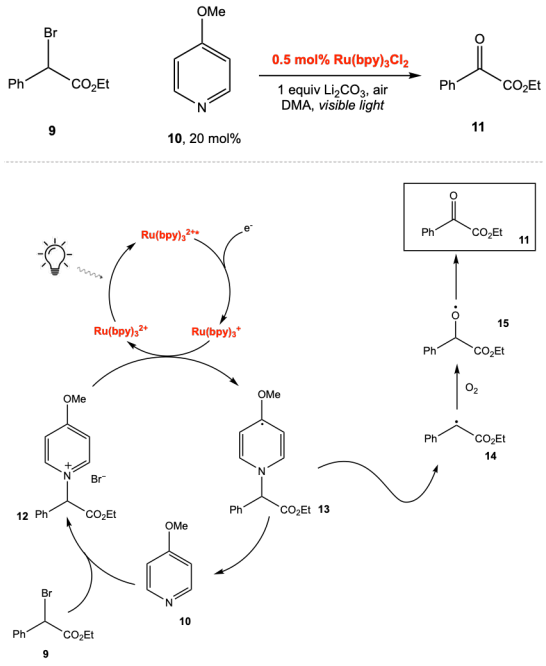

Figure 1.3: Proposed mechanism of aerobic oxidation of benzylic halides redrawn from [13].

In contrast to the reaction types above, photoredox catalysis in redox neutral reactions

has also emerged. In these reactions, both a single-electron oxidation and a single-electron reduction of the substrate occur at different points in the reaction mechanism. In the end, no net oxidation state changes between substrates and products, and no stoichiometric electron donor/acceptor is necessary to turn over the photocatalytic cycle. In this regard, atom transfer radical addition (ATRA) reactions can serve as a typical example, which commonly adopts haloalkanes as the atom transfer reagents and transition metals as catalysts [14, 15]. In addition to ATRA reactions, radical addition to arenes [16, 17], various types of cycloadditions [18–21], and so on have also been reported under redox neutral conditions in recent years.

Besides the photoredox chemistry involving electron transfer between photoexcited catalysts and organic molecules, another fundamental decay pathway of photoexcited states is energy transfer. $Ru(bpy)_3^{2+}$ can again serve as a good example. As shown in Figure 1.4, upon irradiation, $Ru(bpy)_3^{2+}$ excites from its ground singlet state (S_0) to its lowest singlet excited state (S_1), followed by rapid intersystem crossing (ISC) to generate the long-lived lowest-energy triplet state (T_1). Instead of electron transfer, this triplet excited state of $Ru(bpy)_3^{2+}$ can then engage in a triplet-triplet energy transfer (TTET) process, in which $Ru(bpy)_3^{2+*}$ decays back to its ground singlet state while promotes another molecule A from its ground singlet state S_0 to its lowest-energy triplet state T_1 [4]. The approach of TTET from visible light photocatalysts has drawn increasing attention and been used to achieve a considerable amount of organic transformations in recent years [22–26].

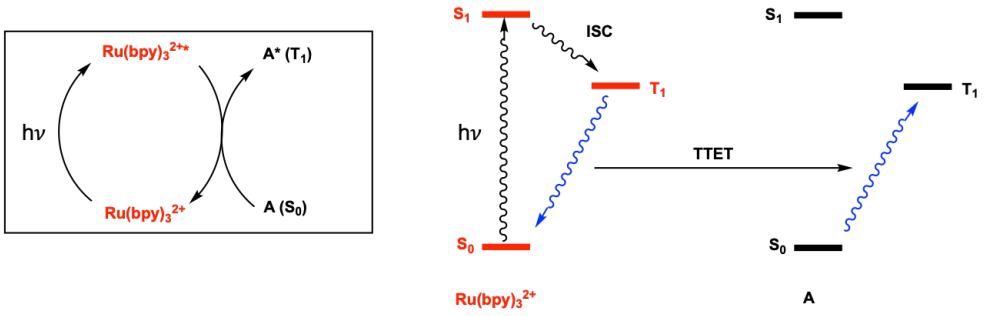

Figure 1.4: Triplet-Triplet Energy Transfer from $Ru(bpy)_3^{2+*}$ to acceptor A. Redrawn from [4].

Although many of the current photoredox applications are based on well-known Ru^{II} polypyridine and cyclometalated Ir^{III} complexes, there is also growing interest in developing new photoredox catalysts based on coordination compounds of Mo^0, Cr^{III}, Re^I, and so on [27]. Overall, photoredox catalysis has been proven to be a valuable tool in regard to the construction of complex molecules, while how to systematically gain mechanistic insights to benefit future catalyst-design remains as the next challenge for researchers.

1.2 Mechanistic Questions

Much progress has been made in the photoredox catalysis with transition-metal complexes over the past few decades in organic synthesis [4, 8, 27]. The motivation of this project, however, is mainly due to the fact that current development of photoredox catalytic protocols still heavily relies on the empirical screening for optimal reaction conditions. Obviously, such lack of rationale will result in a waste of time and material. To develop more efficient synthetic strategies applicable to a broad range of substrates, it is essential to identify the critical mechanistic steps that lead to low product yield. In order to study what causes such differences, we should ask ourselves two questions: (1) Why do certain reaction conditions give higher yields of product than others? (2) What physicochemical characteristics of a given system influence its substrate scope? To answer these questions, we purpose to use infrared absorption spectroscopy to probe these reactions in-situ, and thus can potentially reveal how energy- and/or electron-transfer events are related to desired and undesired bond transformations. Time resolved infrared spectroscopy has demonstrated its ability to site-specifically bond transformations [28, 29], and therefore uniquely qualify for probing reaction kinetics in complex reaction conditions. The goal of this project is to construct an appropriate instrument that allows for this application.

Chapter 2

Methods for Probing Photoredox Catalytic Reactions

2.1 Infrared Absorption Spectroscopy

In order to probe the dynamics of a reaction in-situ, infrared absorption spectroscopy is used to determine the absorbance bands that are unique to individual reaction components. In reality, molecules are not composed of stationary particles with certain distances from each other. On the contrary, they are in constant movement, similar to a spring oscillating about its equilibrium position. Hence, to better understand the molecular vibrations responsible for the characteristic bands observed in infrared spectra, it is helpful to start with a simple model of classical spring-oscillating mechanics [30].

Consider a diatomic molecule with two masses m_1 and m_2 connected by a massless spring. In such a system, each mass oscillates along the axis with different amplitudes, yet both atoms share the same frequency to pass their equilibrium positions,

$$\nu = \frac{1}{2\pi}\sqrt{K(\frac{1}{m_1}+\frac{1}{m_2})} \tag{2.1}$$

where K is the force constant in dynes/cm, m_1 and m_2 are the masses in grams, and ν is the frequency in cycles per second. This expression is also encountered using the *effective mass* where $\frac{1}{m_{\text{eff}}} = \frac{1}{m_1} + \frac{1}{m_2}$ or $m_{\text{eff}} = \frac{m_1 m_2}{m_1+m_2}$. In vibrational spectroscopy, however, wavenumber is more typically used,

$$\overline{\nu} = \frac{1}{2\pi c}\sqrt{K\frac{1}{m_{\text{eff}}}} \tag{2.2}$$

where $\overline{\nu}$ is in waves per centimeter (cm^{-1}), and c is the speed of light in cm/s. Equation 2.2 indicates that the observed frequency of a diatomic oscillator is a function of (1) the force constant K, which is a function of the bond energy; (2) the effective mass of the two atoms involved in the vibration [31]. Despite that larger molecules in nature would be more complex and thereby require more rigorous calculations, a relationship has been

established between effective mass and frequency/wavenumber under diatomic-oscillator assumption.

For the classical harmonic oscillation of a diatomic, the potential energy (PE) is given by

$$PE = \frac{1}{2}KX^2 \tag{2.3}$$

Equation 2.3 describes that the potential energy of this diatomic system as a function of the distance between the masses, X. Given its parabolic shape, the energy minimum sits at the equilibrium internuclear distance, X_{e}, and the force constant, K, is a measure of the curvature of the potential well near X_{e} [31]. Based upon Equation 2.3, the left part of Figure 2.1 demonstrates the vibrational levels in a potential energy diagram for a quantum mechanical harmonic oscillator. Because molecules can only exist in quantized energy states, as shown in Figure 2.1, vibrational energy is not continuously variable but rather exists in discrete states. These states are equidistant and have energy levels E given by

$$E_v = (v + \frac{1}{2})h\nu \quad \text{and} \quad v = 0, 1, 2, \ldots \tag{2.4}$$

where v is vibrational quantum number that can have only integer values, ν is the classical vibrational frequency of the oscillator, and h is Planck constant. The harmonic oscillator has a zero-point energy of $E = \frac{1}{2}h\nu$ at $v = 0$, and this vibrational energy cannot be removed from the molecule [31]. With selection rules for vibrational transitions applied, a molecule can transit only from one energy state to another at $\Delta v = \pm 1$, which is what is probed by spectroscopy [31].

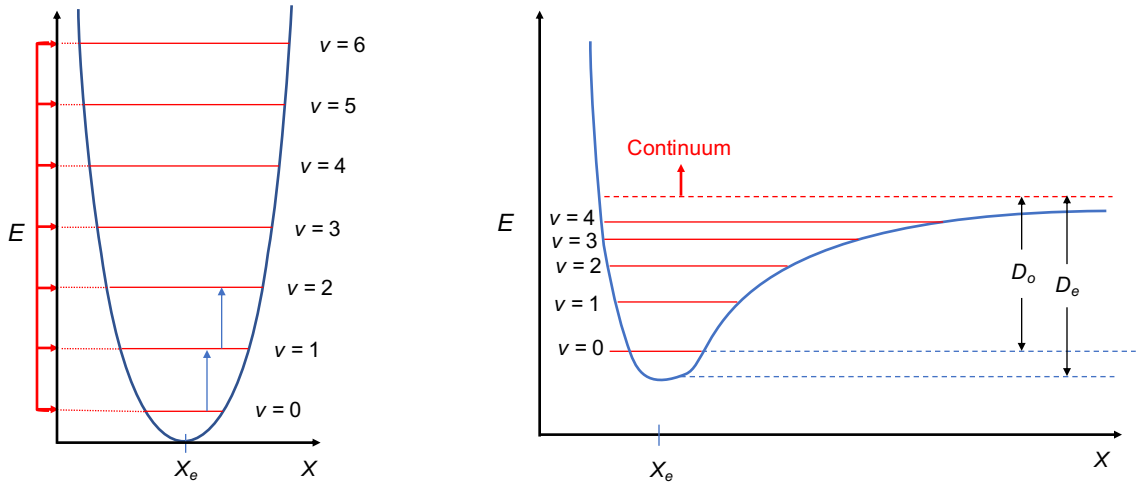

Figure 2.1: **Left**: Potential energy, E, versus internuclear distance, X, for a diatomic harmonic oscillator. **Right**: Potential energy, E, versus internuclear distance, X, for an anharmonic oscillator. Transitions originate from the v = 0 level, and D_o is the energy necessary to break the bond. D_e is the dissociation energy. Modified from [31].

Beyond the harmonic approximation, a more realistic approach is to introduce anharmonicity: the Morse Potential. Anharmonicity results from the change in the dipole moment that is non-linearly proportional to the nuclear displacement coordinate [31]. The right part of Figure 2.1 shows the potential energy level diagram for a diatomic anharmonic oscillator. Under the Morse-oscillator model, the separation between adjacent levels becomes smaller at higher vibrational levels until finally reaches dissociation limit. In the case of the harmonic oscillator, only transitions to adjacent levels, i.e. fundamental transitions ($\Delta v = \pm 1$), are allowed, whereas for the Morse oscillator, overtones ($\Delta v = \pm 2, \pm 3, \ldots$) can also occur. Nevertheless, probability of transitions to higher vibrational states is much smaller than the fundamentals, as well as the intensity of such transitions is much weaker. The exact energy levels of the Morse oscillator are given by

$$E_v = h\nu_e(v + \frac{1}{2}) - h\chi_e\nu_e(v + \frac{1}{2})^2 \tag{2.5}$$

where $\chi_e\nu_e$ defines the magnitude of the anharmonicity [31].

In reality, only when the dipole moment of molecules changes due to the oscillation of the atoms will energy be transferred from the IR photon to the molecule via absorption, i.e. such vibrations are IR-active [31, 32]. The mid-IR (400–4000 cm^{-1}) range coincides with the energies required to excite fundamental stretching and bending normal modes of vibration in molecules. If the electromagnetic field of an incident photon happens to have the same frequency as the dipole oscillating, it will be absorbed [31]. Conclusively, because the absorption bands that correspond to the photon energies required to excite vibrations are unique to each molecule, infrared absorption spectroscopy is often used to probe reaction dynamics and identify existence of chemicals. For transmission infrared absorption spectroscopy, a sample is placed into the IR beam. As the IR beam passes through the sample, the transmitted energy is measured and a spectrum is generated by plotting the intensity (absorbance or transmittance) versus the wavenumber. The relationship between the intensities of the absorbance and the analyte concentration is given by the Lambert-Beer law [33].

2.2 Fourier-Transform Infrared Spectroscopy

In order to monitor transient changes in reaction mixture, Fourier-Transform infrared (FTIR) spectroscopy is adopted in experiments to collect high-spectral/time-resolution data over a wide spectral range. The essential piece in a FTIR spectrometer is the interferometer. A basic scheme of a simplified Michelson interferometer is shown in Figure 2.2. The beam splitter ideally reflects 50% of the incident light onto the fixed mirror and transmits the other 50% of the light to the movable mirror. Because the movable mirror is constantly moving back and forth, as the two light beams recombine on the beam splitter,

the electromagnetic waves that make up the partial beams move in and out of phase. The beam leaving the interferometer passes through the sample compartment and is finally focused on the detector. The detector thus records an interference pattern as a function of the optical path difference (OPD), δ, between the two mirrors, and the intensity I(δ) recorded on the detector is called an interferogram [32, 34].

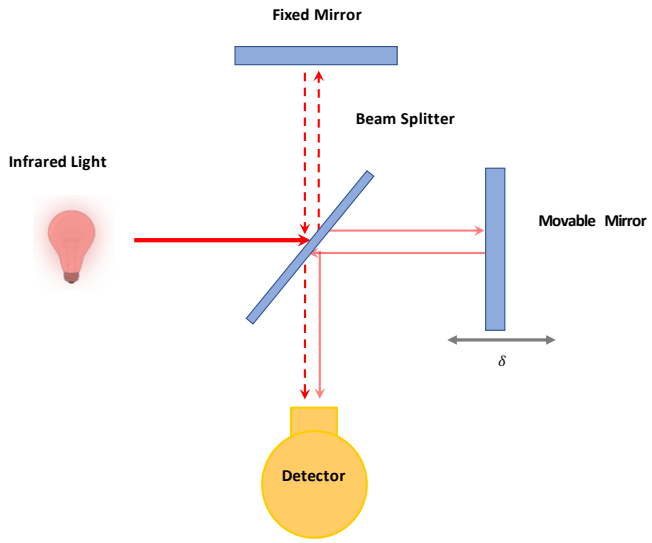

Figure 2.2: A scheme of Michelson interferometer. The beam splitter divides the incident beam into two beams with an optical path difference ($\boldsymbol{\delta}$) that depends on the location of the movable mirror.

For a radiation that has wavenumber $\overline{\nu}$, the intensity of the detected signal due to radiation in the range of wavenumbers $\overline{\nu}$, which can be denoted as I(δ, $\overline{\nu}$)d$\overline{\nu}$, varies with δ as [32]:

$$I(\delta, \overline{\nu})d\overline{\nu} = I(\delta)(1 + \cos(2\pi\overline{\nu}\delta))d\delta \tag{2.6}$$

Hence, the interferometer converts the presence of a particular wavenumber component in the signal into a variation in intensity of the radiation reaching the detector [32]. Equation 2.6 allows precise tracking of the movable mirror. In fact, all FTIR spectrometers use the interference pattern of the monochromatic light of a HeNe laser (632 nm) to control the change in OPD. Every time the laser detector reads zero intensity, the reading on the IR detector is digitized. This results in an interferogram, i.e. the IR intensity as a function of OPD. The accuracy of the sample spacing between two zero crossings is only determined by the precision of the laser wavelength itself. Hence, FTIR spectrometers have a built-in wavenumber calibration of high precision, practically about 0.01 cm^{-1} [34].

A real signal includes radiation with a wide range of wavenumbers, and the total intensity at the detector, I(δ), is the sum of contributions from all the wavenumbers present in the signal [32]:

$$I(\delta) = \int_0^\infty I(\delta, \overline{\nu}) d\overline{\nu} = \int_0^\infty I(\overline{\nu})(1 + \cos(2\pi\overline{\nu}\delta)) d\overline{\nu} \tag{2.7}$$

The next problem is to find the variation of intensity with wavenumber, I($\overline{\nu}$), from detected values of I(δ). This step is the 'Fourier transformation' step, which gives the spectral intensity distribution of the IR light:

$$I(\overline{\nu}) = 4 \int_0^\infty \{I(\delta) - \frac{1}{2} I(0)\} \cos(2\pi\overline{\nu}\delta) d\delta \tag{2.8}$$

where I(0) is given by Equation 2.7 with δ = 0. The output, I($\overline{\nu}$), is the transmission spectrum of the sample.

Typically, an infrared spectrum of a sample is collected in a two-step process: (1) Collect the spectral intensity distribution without a sample or with some reference sample in the beam path. This is the *single beam reference*, $I_{ref}(\nu)$. (2) Collect the spectral intensity distribution with the sample in the beam path. This is the *single beam sample*, $I_s(\nu)$. The transmission spectrum is given by

$$T(\nu) = \frac{I_s(\nu)}{I_{ref}(\nu)} \tag{2.9}$$

and often the case, absorbance units are preferred:

$$A(\nu) = -log[T(\nu)] = -log[\frac{I_s(\nu)}{I_{ref}(\nu)}] \tag{2.10}$$

2.3 Step-Scan versus Rapid-Scan FTIR

Transient time-resolved studies commonly use FTIR spectroscopy due to its throughput and multiplex advantages in comparison to other dispersive spectroscopies [35]. Specifically, step-scan and rapid-scan are two different operating modes in FTIR spectroscopy, both with advantages and drawbacks. This section provides a comparison between these two operating modes, and briefly discusses how we adopt mainly step-scan FTIR in our experimental design.

As shown in Figure 2.2, a simplified Michelson interferometer contains two mirrors: one mirror is held in a fixed position relative to the beamsplitter during the measurement, whereas the other mirror scans back and forth. In a rapid-scan FTIR then, the moving mirror moves forward and backward in a rapid continues fashion. In this case, the time resolution is determined by the difference between two successively acquired interferograms, and the temporal resolution is therefore limited by the speed that the moving mirror can achieve [36]. In fact, currently even the fastest conventional interferometers can achieve only approximately 100 spectra/sec at 10 cm^{-1} spectral resolution, resulted in time

resolution to only 10 ms [36]. Moreover, as the spectral resolution is increased, the OPD becomes greater, and the moving mirror takes longer time in return to complete one scan. Thus, rapid-scan FTIR is intrinsically limited in the temporal resolution, especially at high spectral resolution [36].

In step-scan FTIR, however, time resolution is dramatically improved because it is no longer limited by the scan rate. Briefly, the moving mirror now is translated in discrete steps rather than in a continuous fashion [35]. At each position, a reproducible experiment is initiated and the IR light intensity is recorded at desired equi-spaced time intervals. Once a recording is complete, the mirror is then stepped to the next position, and the experiment is initiated again. In other words, every time at a step position, with the moving mirror holding still, a new experiment is initiated, and the IR light intensity is digitized at desired time resolution, until the time-varying intensities are recorded for a complete set of mirror positions [36]. Figure 2.3 serves as an example to demonstrate this whole process, where the optical path difference δ is on the x-axis, the intensity is on the y-axis, and time is on the z-axis going into the page. As shown, intensity changes of an exponential decay in time has been digitized and recorded at each mirror position. At the end of the step-scan experiment, the digitized intensity data have been transposed into interferograms corresponding to different times after trigger, and subsequently Fourier transformed to yield a series of time-resolved spectra [35].

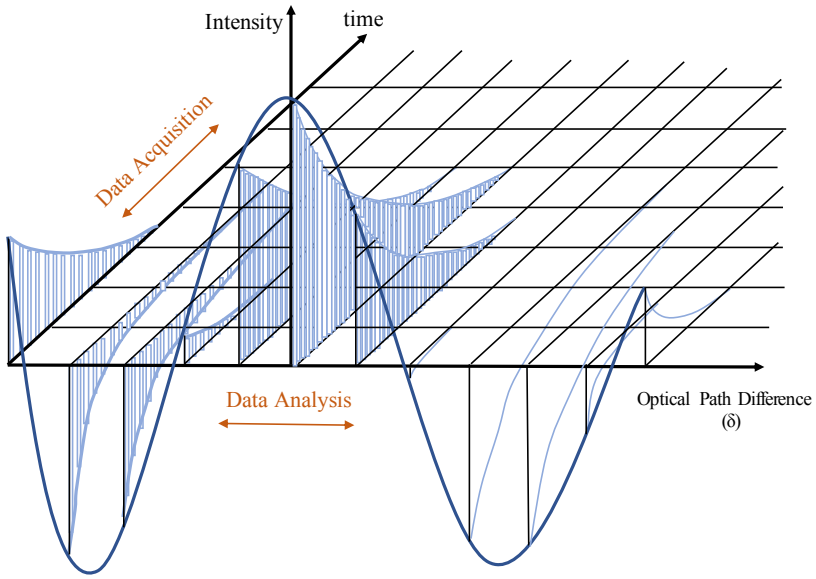

Figure 2.3: Schematic diagram of data acquisition and data analysis in Step-Scan FTIR redrawn from [36]. The transient data are recorded as a function of time at mirror position 1, then mirror position 2, etc., and then followed up by a transpose to generate interferograms.

Despite that step-scan FTIR can apply to only reproducible experiments, and the total

experiment time is extensively longer comparing to rapid-scan, the major advantage is that the achievable time resolution is limited no longer by the scan rate of the moving mirror, but only by the response speed of the detector and acquisition electronics, as well as by the detector sensitivity [35, 36]. Considering that the lifetime of the triplet state of the light absorber is on the order of a sub-microsecond [37], adopting step-scan FTIR to monitor reaction dynamics is therefore necessary. The MCT detector used in our transient infrared pump-probe setup has a 22 ns rise time, combined with a 14-bit transient recording board serving as a digitizer. Overall the time resolution in our step-scan system can achieve as high as 25 ns. Such a time resolution is more than an order of magnitude higher than the lifetime of the interested intermediates, and thereby should allow for sensitive probing of reactions in-situ.

Chapter 3

Construction of Step-Scan Pump-Probe FTIR Setup

3.1 Experimental Components

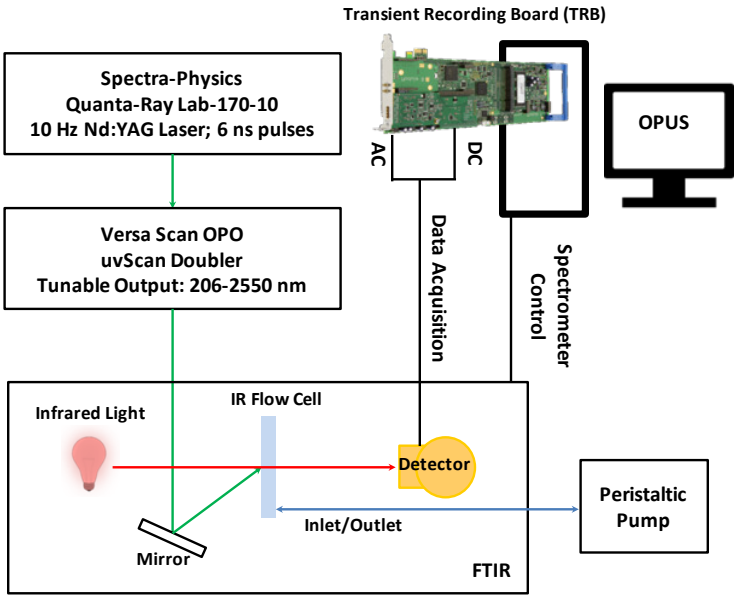

Figure 3.1: Schematic diagram of complete experimental setup.

The complete visible-pump/IR probe experimental setup is demonstrated in Figure 3.1. A Nd:YAG laser system (Spectra-Physics; Quanta-Ray Lab-170-10 with VersaScan OPO and uvScan Doubler; repetition rate: 10 Hz; pulse width: 6 ns) serves as an excitation source. Laser light first passes an optical parametric oscillator (OPO), which can tune the light wavelength as needed. Next, laser light is reflected by mirrors and then focused on the sample solution in the IR flow cell. Meanwhile, a beam of infrared light shoots out from a Bruker Vertex 70 FTIR spectrometer (Billerica, MA) to the sample and then is

recorded by a photovoltaic Mercury Cadmium Telluride (MCT) detector (Kolmar Technologies; KMPV11-1-J1/DC) detector. A peristaltic pump (Watson-Marlow; 120U/D1) continuously circulates sample solution in and out of the IR flow cell to avoid potential photodamage by the laser. During experiment, signal from the detector is concurrently recorded in two channels, AC channel and DC channel, and both are digitized on a 14-bit transient recording board (Spectrum Instrumentation; M3i-4142-exp) installed in the computer. A software called OPUS is used to control spectrometer and to do all the experiments. A detailed description of each important component is discussed in the following sections.

3.1.1 Laser

Laser is an acronym derived from Light Amplification by Stimulated Emission of Radiation, which is an oscillating amplifier of light. The output of laser comprises photons that are identical in phase and direction, its output beam thereby is singularly directional, monochromatic, and coherent. A laser is designed to take advantage of absorption, and both spontaneous and stimulated emission phenomena, together to create conditions favorable to light amplification.

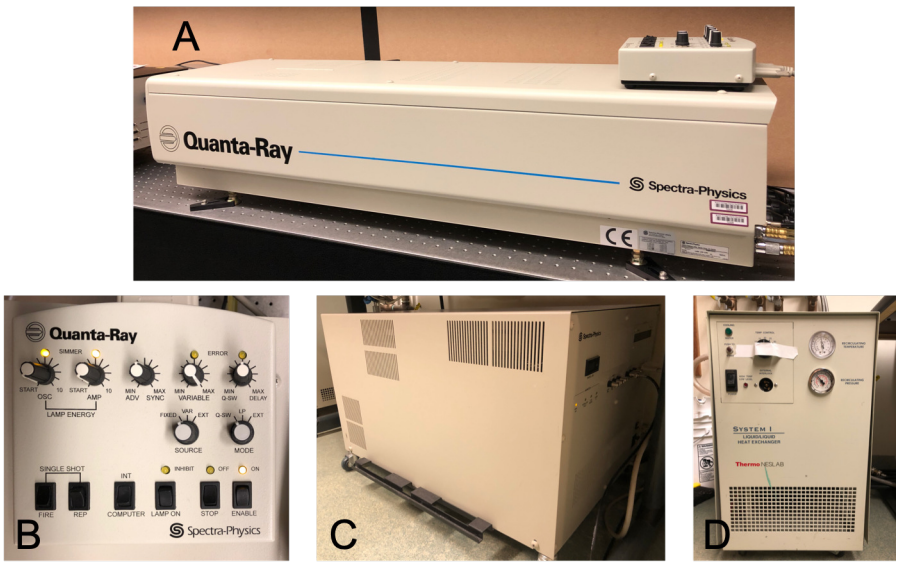

Figure 3.2: Overview of Laser system. **A**: Laser Head, **B**: Controller panel, **C**: Power supply, **D**: Heat exchanger

The Nd:YAG laser system, which consists a laser head, a controller panel, and a power supply (Figure 3.2), is used as the light source to pump photocatalytic systems. The laser head contains the optical resonator, Nd:YAG lasing medium, oscillator flash lamps, harmonic generator and output routing mirrors. It can be easily set and controlled for various

system parameters by the conventional knobs and switches on the table-top controller. The power supply is water cooled and requires an external source of clean cooling water. Additional water-to-air heat exchanger is also necessary for this purpose [38]. During experiment process, a 5 V TTL signal that comes out from the laser triggers the transient recording board via BNC connection to initiate spectroscopic measurement at each step position.

3.1.2 FTIR Spectrometer

The transmission infrared spectra are obtained using a Bruker Vertex 70 FTIR spectrometer (Billerica, MA) and a photovoltaic MCT detector. A top view of the spectrometer with each compartment indicated is shown in Figure 3.3. The compartment of detector, interferometer, and the beam direction control are not separated from each other but form a uniform compartment. All spectrometer compartments are accessible by opening or removing the corresponding cover [39]. The sample compartment can be accessed from the front side of the spectrometer. For the convenience of our experiments, the sample compartment cover has been removed in order to install and closely monitor the IR flow cell (Figure 3.4). The basic spectrometer configuration is equipped a MIR source, which is an U-shaped silicon carbide globar that emits mid-infrared light [39]. With this source, spectroscopic measurements in the mid-infrared region can be performed.

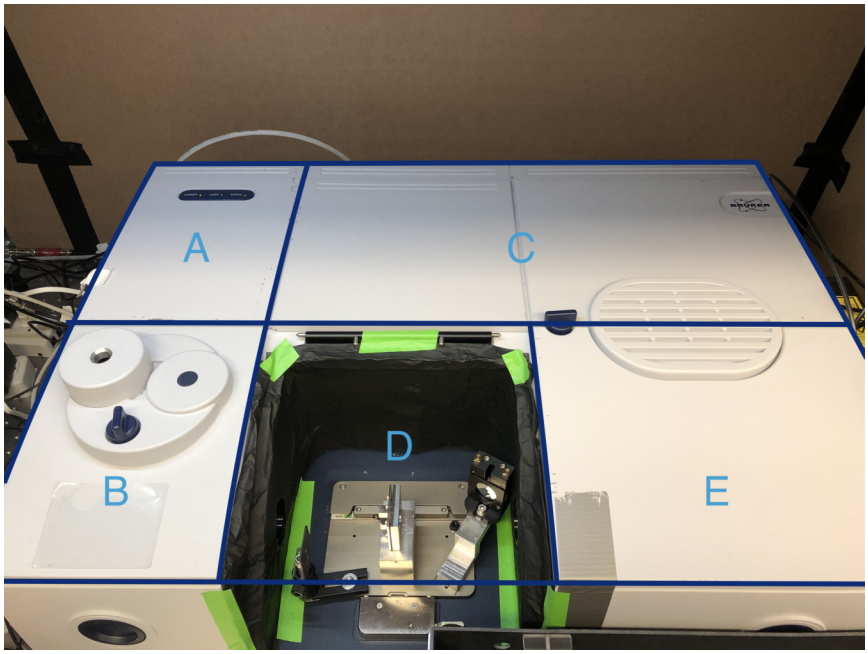

Figure 3.3: General overview of Vertex 70 FTIR spectrometer (Top view). **A**: Electronics compartment, **B**: Detector compartment, **C**: Interferometer compartment, **D**: Sample compartment, **E**: Beam direction control compartment

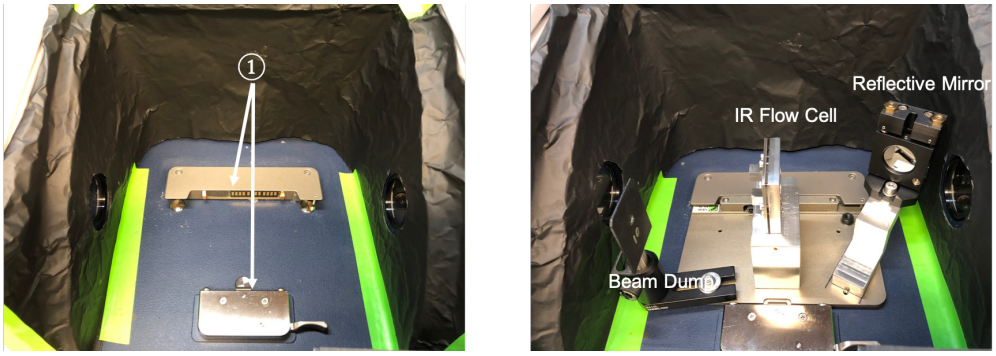

Figure 3.4: The sample compartment is equipped with a QuickLock locking mechanism ① , which allows for an exact and reproducible positioning of the accessory in the sample compartment.

3.1.3 MCT Detector

A detector converts radiation into an electric current or voltage for appropriate signal processing and display [32]. In our experiments, a photovoltaic MCT detector (Kolmar Technologies; KMPV11-1-J1/DC; rise time: 22 ns; liquid N_2 cooled) is installed in the Vertex 70 FTIR spectrometer for signal recording. It contains a high-speed photodiode with integral pre-amplifier in pour filled Dewars. A germanium window is set in front of the detector to cut off light above 2200 cm^{-1}. Originally, the output can be ordered as either DC or AC. For our experiments, the output signal has been split up to two channels. Both are then digitized by the transient recording board, and thereby allows concurrent AC-coupled and DC-coupled recording.

3.1.4 Electronics

In step-scan transient spectra, the time-dependent intensity changes are a few orders of magnitude smaller than the static intensity. Hence, in order to optimize signal sensitivity, a key step in our pump-probe experiment is to simultaneously record AC-coupled and DC-coupled signals. The signal sensitivity, i.e. resolution, is calculated as:

$$Resolution = \frac{InputRange}{2^{\text{bit}}} \tag{3.1}$$

This means there are two ways to improve resolution: a smaller input range, or a higher bit of a digitizer. However, for a specific digitizer, in our case the transient recording board, the bit is fixed. Therefore, the only way to improve resolution is to have a smaller input range. For digital signals like ours, most of them contain both AC and DC components. The DC component acts as an offset in the time domain, whereas the AC component consists of all other frequencies. If only DC-coupled signal is recorded, it would require a

larger input range to cover the DC offset, resulting in low resolution. As a result, to digitize with maximum sensitivity, it is advantageous to AC-couple the detector, and a common solution to do so is by adding an **electronic filter** to remove DC offset.

However, AC coupling also brings one problem. The original spectra contain only positive intensities. Once AC-couple the detector, the resulting signals contain both **positive** and **negative** intensities, which will not be processed correctly by the standard Mertz and Forman [40, 41] phase correction algorithms. The standard algorithms assume that most of the intensity in the spectrum is positive. When negative intensities are present, they are likely to be mis-interpreted as positive intensities with a phase shift of π radians [42, 43]. To solve phase errors caused by mis-interpretation, alternative phase correction method is necessary. A commonly used method is to measure a simultaneously recorded DC-coupled interferogram, from which the phase information can be extracted and applied to AC-coupled signal for phase correction.

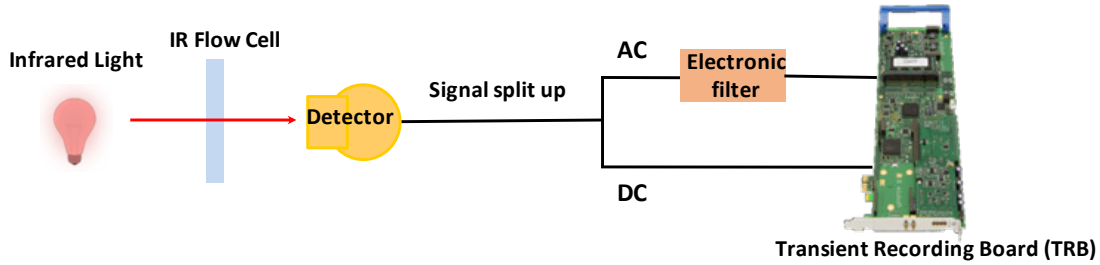

Figure 3.5: Schematic diagram of connection between detector and transient recording board.

In a word, as shown in Figure 3.5, signal that comes out from the detector is split up by a T-shaped BNC adaptor to two channels, AC channel and DC channel, which are then both connected to the transient recording board. An additional electronic filter, EF500 from Thorlabs, is included in AC channel via BNC connection. The design of EF500 extends the low end of the 1 dB passband to 1 Hz in a BNC coaxial package, i.e. only signal with frequency higher than 1 Hz can pass, therefore can effectively filter out the 0 Hz DC offset and in return to optimize the signal sensitivity. For the consequent phase-error issue, the signal concurrently recorded in DC channel will provide accurate phase information to correct AC-coupled signal. To test the functionality and reliability of this setup, a series of chopper wheel experiments was conducted and discussed in a later section.

3.1.5 Flow Cell

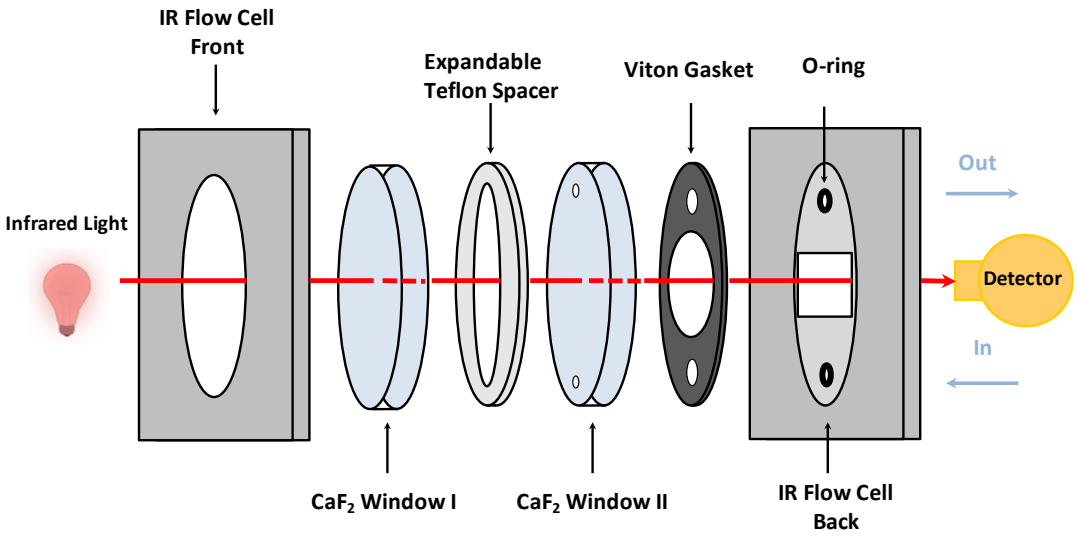

Figure 3.6: Schematic design of IR flow cell.

An IR flow cell was specifically designed for this project. As demonstrated in Figure 3.6, it contains two metal components as its front and back, which can be tightly screwed together for assembling. Two CaF_2 windows allow both laser and Infrared light to pass through. In between is an expandable Teflon spacer with an oval-shaped hole in the center, which requires 0.2 mL of solution to fill up. A Viton gasket is kept in between of the CaF_2 window II and the metal back part to release pressure from the metal against the window to avoid possible breakage of the window. Once the flow cell is assembled and set ready for experiments, a peristaltic pump will continuously pump solution in and out through the cell. A beam of infrared light will shoot out from the front of the cell, pass through it, and then be received by the detector to record signals.

3.2 Experimental Results

3.2.1 Pump-Probe Experiment of $Ru(bpy)_3^{2+}$

Ruthenium(II)-trisbipyridine is a d^6 transition metal complex with octrahedral geometry. A simplified molecular orbital diagram of $Ru(bpy)_3^{2+}$ is shown in Figure 3.7 along with its ground state absorption spectrum. When ruthenium forms complexes with polypyridine ligands, the formed molecular orbitals will be localized either mainly on the metal or on the ligands. Several absorption bands that appear in the ground state absorption spectrum correspond to different types of transitions between the molecular orbitals in the complex:

metal-to-ligand charge transfer (MLCT) transition, metal centered (MC) transition, and ligand centered (LC) transition. Which transition will be lowest in energy depends on the oxidation state of the metal center, as well as on the nature of the ligands. For most Ru(II)-complexes with polypyridine type ligands, however, ^{1}MLCT transition has the lowest energy, and the corresponding lowest excited states are the ^{3}MLCT states [44]. Such transition describes that one of the valence electrons in the t_{2g} (π_M) orbital, the highest occupied molecular orbital (HOMO) in the ground state, is excited at wavelength within the ^{1}MLCT absorption region, and then transferred to the π^* orbital of the ligands.

$Ru(bpy)_3^{2+}$ has been utilized in various research fields as a photosenzitizer during the last 30 years due to its fabulous photochemical properties [44, 45]. As shown in Figure 3.7, absorbance in both the visible and UV regions is high. In the excited state, lifetime of $Ru(bpy)_3^{2+}$ is reported to be 0.89 ± 0.03 μs (acetonitrile) [37], long enough to be used in bimolecular electron or energy transfer reactions. Due to these advantages of $Ru(bpy)_3^{2+}$, as well as its readily available data and spectra resources, $Ru(bpy)_3^{2+}$ was chosen as a model-molecule to conduct the pump-probe experiment and test the functionality of our experimental setup.

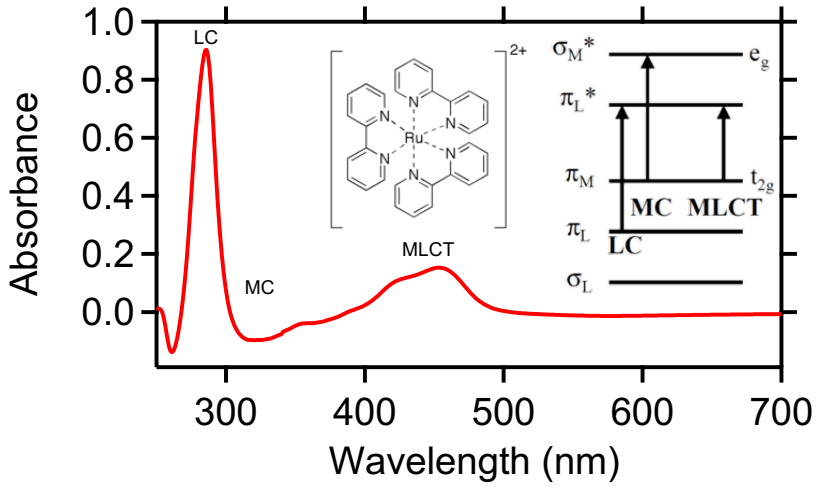

Figure 3.7: UV-Vis absorption spectrum of $Ru(bpy)_3^{2+}$ together with a simplified molecular orbital diagram.

A detailed experimental procedure of preparing a sample solution was carried out as follows. About 0.150 gram of Tris(2,2-bipyridyl)dichlororuthenium(II) hexahydrate (TCl America, Fisher Scientific) was dissolved in 20 mL of Acetonitrile-*d3* (Acros Organics, Fisher Scientific) to give a concentration of 10 mM. The solution was then sonicated for 30 min to achieve homogeneous mixing. Once mixed well, the sample solution was transferred to a reservoir and deoxygenated by sparging with argon for 15 min before experiments started.

Both ground-state and time-resolved infrared (TRIR) spectra were recorded for $Ru(bpy)_3^{2+}$ and are shown in Figure 3.8. For ground-state spectrum, the interferometer was operated in the conventional rapid-scan mode with spectral resolution of 4 cm^{-1} to record single beam spectra of both pure Acetonitrile-*d3* and of sample solution. For TRIR spectrum, laser was set to an exciting wavelength of 355 nm, and the interferometer was operated in the step-scan mode with various spectral resolutions. Due to signal-to-noise consideration, as well as consultation from literature [46], all spectra were taken at sampling window 700–2400 cm^{-1}. From ground-state spectrum on the left in Figure 3.8, matching ground-state bands from our result to the literature were observed and denoted. For TRIR spectrum, excited state bands and bleaching were not as clear at low spectral resolution of 8 cm^{-1}. Nevertheless, as spectral resolution improved to 4 cm^{-1}, better signal matching to the literature was observed and denoted. Please note that in TRIR spectra, the magnitude of transient signal is unusually high instead of a much smaller change supposedly associated to the low concentration of the intermediate. This is possibly due to light scattering, and further investigation is required for this issue.

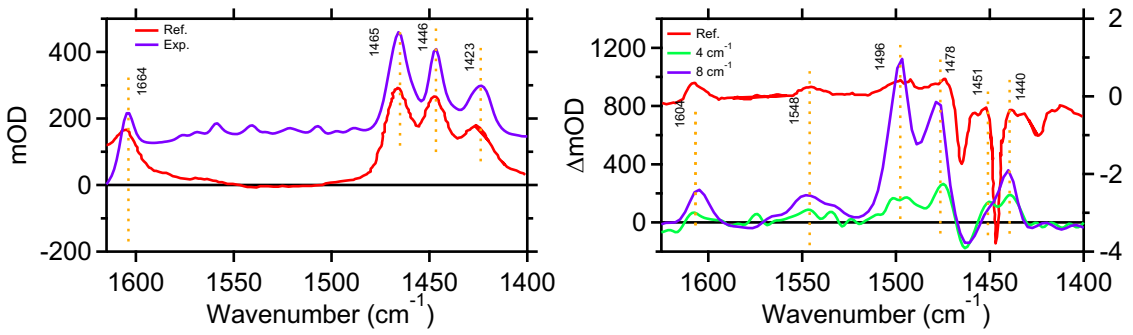

Figure 3.8: **Left**: Comparison of experimental ground-state spectrum of $Ru(bpy)_3^{2+}$ with Omberg *et al.* [46]. **Right**: Comparison of experimental time-resolved Infrared (TRIR) spectra of $Ru(bpy)_3^{2+}$ with Omberg *et al.* [46] .

Furthermore, to study the lifetime of $Ru(bpy)_3^{2+}$, we did an exponential decay fitting by replotting the signal intensity against time. As shown in Figure 3.9, the optimized experimental lifetime is 0.325 ± 0.072 μs. The reason why experimental lifetime is less than one half of 0.89 ± 0.03 μs reported in literature [37] is possibly due to that tubing for solution pumping is permeable to O_2, thus O_2 left in the reaction system shortens the lifetime. In addition, local temperature rising due to laser pulse heating is also possibly accountable for shortened lifetime. Nevertheless, the experimental and reported lifetime agree in the same order of magnitude, indicating the potential of our experimental setup to closely monitor transient reaction dynamics in-situ. With more effective sealing and degassing methods, both precision and accuracy of our experimental results will be significantly improved.

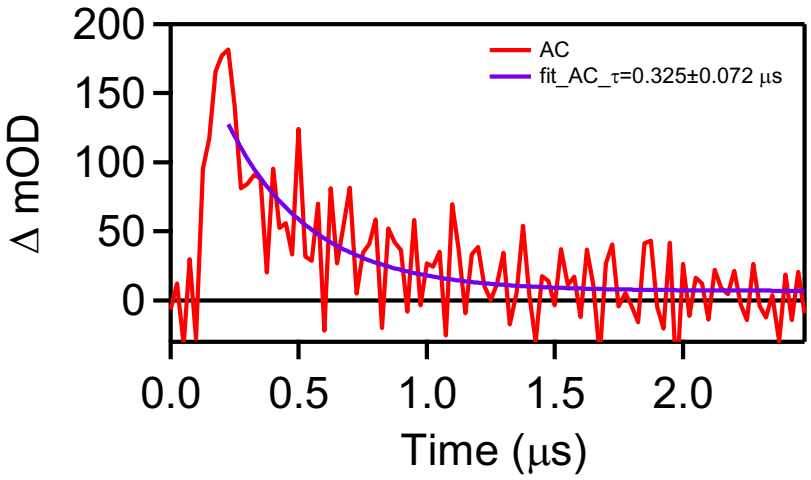

Figure 3.9: Optimized exponential decay fitting of $Ru(bpy)_3^{2+}$*. Fitted lifetime for phase-corrected AC-coupled signal is 0.325±0.072 μs.

3.2.2 Chopper Wheel Experiment

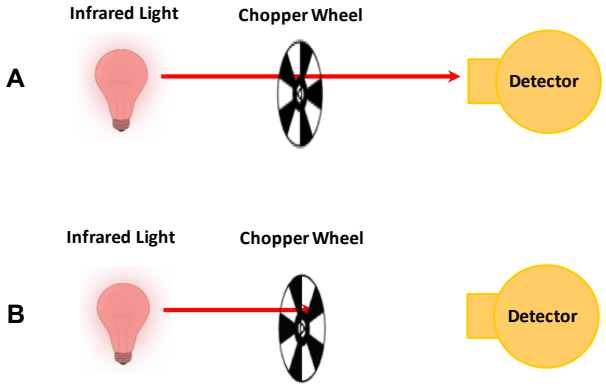

Figure 3.10: Scheme of Chopper Wheel Experiment. **A**: When infrared light passes through chopper wheel, signal is detected. **B**: When infrared light is blocked by chopper wheel, no signal is detected.

To test for signal sensitivity improvement and phase correction, we designed a chopper wheel experiment. As shown in Figure 3.10, a chopper wheel was placed in the IR beam path. As it rotated about its center, the infrared beam either passed through it and arrived at the detector, or was blocked by the chopper and thereby no signal was detected. The experimental protocol was to set up chopper wheel experiments with input range of ±**500 mV** and ±**1 V**, respectively. The option of ±**500 mV** is the smallest input range that OPUS

allows, and experimental results from input range of $\pm$**1 V** are used as a control group to analyze drop of signal amplitude. Once experiments were finished, signal intensity was plotted against time, and a square-wave like signal was expected to observe.

Initial results without phase correction are shown in Figure 3.11. By comparing DC and AC signals, one can clearly tell that DC offset has been removed after adding an electronic filter. Furthermore, as expected, results from input range of $\pm$500 mV and $\pm$1 V form strong contrast: amplitude drops significantly as input range increases, confirming that larger input range would lower signal resolution. Lastly, negative waves are now missing from AC signal, indicating phase errors.

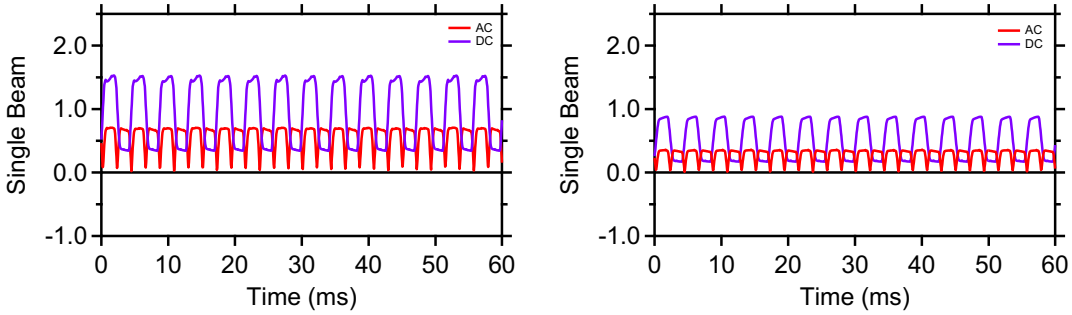

Figure 3.11: Initial results without phase correction. **Left**: Results of input range of $\pm$500mV. **Right**: Results of input range of $\pm$1V.

In order to solve phase-error problem, the phase information from the simultaneously recorded DC-coupled interferogram was extracted, and then was applied to AC-coupled signal for phase correction. Results after correcting are shown in Figure 3.12: AC-coupled signal not only has removed DC offset, but also obtained correct phase now.

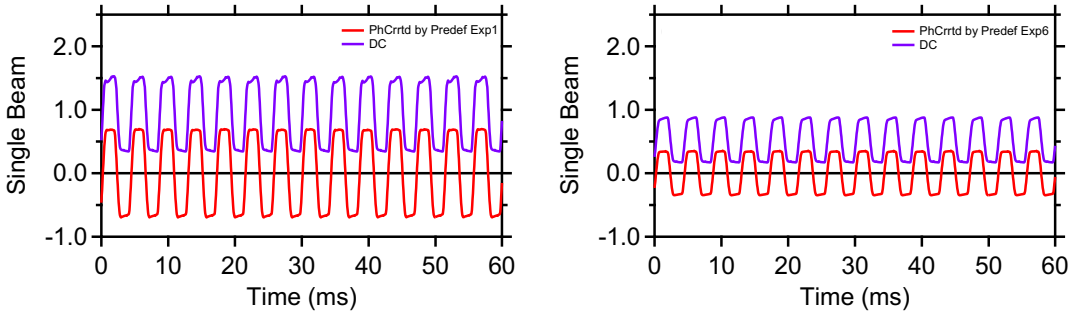

Figure 3.12: Results after phase correction. **Left**: Results of input range of $\pm$500mV. **Right**: Results of input range of $\pm$1V.

The encouraging results from chopper wheel experiment indicate following conclusions. First, without DC offset, smallest input range can be applied to AC-coupled signal,

in return will give optimized spectral resolution. Second, successful correcting method to phase-error problem assures that AC-coupled signal is reliable.

3.3 Conclusions

This research project proposes to mainly utilize step-scan FITR probe photoredox catalytic reactions in-situ, and thus can potentially reveal how energy- and/or electron-transfer events are related to desired and undesired bond transformations and thus illuminate future directions in regard to catalyst-design. To fulfill research objectives, a transient infrared pump-probe setup has been designed and fully constructed as illustrated in Figure 3.1. A series of initial trials has been conducted for testing purpose. Results from pump-probe experiment of $Ru(bpy)_3{}^{2+}$ have demonstrated its reliable functionality, and results from chopper wheel experiment have further confirmed that signal sensitivity has been optimized, and the phase-error problem has been solved successfully. Since experimental results fulfill the expectations and thereby support further investigations in reaction dynamics, applying this transient infrared pump-probe setup to suitable hypothesis-driven case studies can be future goal for the next stage.

Bibliography

1. Prihod'ko, R. V. & Soboleva, N. M. Photocatalysis: oxidative processes in water treatment. *Journal of Chemistry* **2013** (2013).
2. Armaroli, N. & Balzani, V. Solar electricity and solar fuels: status and perspectives in the context of the energy transition. *Chemistry–A European Journal* **22,** 32–57 (2016).
3. Ciamician, G. The photochemistry of the future. *Science* **36,** 385–394 (1912).
4. Prier, C. K., Rankic, D. A. & MacMillan, D. W. Visible light photoredox catalysis with transition metal complexes: applications in organic synthesis. *Chemical reviews* **113,** 5322–5363 (2013).
5. Nicewicz, D. A. & MacMillan, D. W. Merging photoredox catalysis with organocatalysis: the direct asymmetric alkylation of aldehydes. *Science* **322,** 77–80 (2008).
6. Zuo, Z., Ahneman, D. T., Chu, L., Terrett, J. A., Doyle, A. G. & MacMillan, D. W. Merging photoredox with nickel catalysis: Coupling of α-carboxyl sp^3-carbons with aryl halides. *Science* **345,** 437–440 (2014).
7. Theriot, J. C., Lim, C.-H., Yang, H., Ryan, M. D., Musgrave, C. B. & Miyake, G. M. Organocatalyzed atom transfer radical polymerization driven by visible light. *Science* **352,** 1082–1086 (2016).
8. De Abreu, M., Belmont, P. & Brachet, E. Synergistic Photoredox/Transition-Metal Catalysis for Carbon–Carbon Bond Formation Reactions. *European Journal of Organic Chemistry* (2019).
9. Takeda, H. & Ishitani, O. Development of efficient photocatalytic systems for CO_2 reduction using mononuclear and multinuclear metal complexes based on mechanistic studies. *Coordination Chemistry Reviews* **254,** 346–354 (2010).
10. Blanksby, S. J. & Ellison, G. B. Bond dissociation energies of organic molecules. *Accounts of chemical research* **36,** 255–263 (2003).
11. Kalyanasundaram, K. Photophysics, photochemistry and solar energy conversion with tris (bipyridyl) ruthenium (II) and its analogues. *Coordination Chemistry Reviews* **46,** 159–244 (1982).

12. Pac, C., Ihama, M., Yasuda, M., Miyauchi, Y. & Sakurai, H. Tris (2, 2'-bipyridine) ruthenium (2+)-mediated photoreduction of olefins with 1-benzyl-1, 4-dihydronicotinamide: a mechanistic probe for electron-transfer reactions of NAD (P) H-model compounds. *Journal of the American Chemical Society* **103,** 6495–6497 (1981).

13. Su, Y., Zhang, L. & Jiao, N. Utilization of natural sunlight and air in the aerobic oxidation of benzyl halides. *Organic letters* **13,** 2168–2171 (2011).

14. Nguyen, J. D., Tucker, J. W., Konieczynska, M. D. & Stephenson, C. R. Intermolecular atom transfer radical addition to olefins mediated by oxidative quenching of photoredox catalysts. *Journal of the American Chemical Society* **133,** 4160–4163 (2011).

15. Wallentin, C.-J., Nguyen, J. D., Finkbeiner, P. & Stephenson, C. R. Visible light-mediated atom transfer radical addition via oxidative and reductive quenching of photocatalysts. *Journal of the American Chemical Society* **134,** 8875–8884 (2012).

16. Kalyani, D., McMurtrey, K. B., Neufeldt, S. R. & Sanford, M. S. Room-temperature C–H arylation: merger of Pd-catalyzed C–H functionalization and visible-light photocatalysis. *Journal of the American Chemical Society* **133,** 18566–18569 (2011).

17. Furst, L., Matsuura, B. S., Narayanam, J. M., Tucker, J. W. & Stephenson, C. R. Visible light-mediated intermolecular C- H functionalization of electron-rich heterocycles with malonates. *Organic letters* **12,** 3104–3107 (2010).

18. Zhao, G., Yang, C., Guo, L., Sun, H., Lin, R. & Xia, W. Reactivity Insight into Reductive Coupling and Aldol Cyclization of Chalcones by Visible Light Photocatalysis. *The Journal of Organic Chemistry* **77,** 6302–6306 (2012).

19. Ischay, M. A., Ament, M. S. & Yoon, T. P. Crossed intermolecular [2+ 2] cycloaddition of styrenes by visible light photocatalysis. *Chemical science* **3,** 2807–2811 (2012).

20. Hurtley, A. E., Cismesia, M. A., Ischay, M. A. & Yoon, T. P. Visible light photocatalysis of radical anion hetero-Diels–Alder cycloadditions. *Tetrahedron* **67,** 4442–4448 (2011).

21. Maity, S., Zhu, M., Shinabery, R. S. & Zheng, N. Intermolecular [3+ 2] cycloaddition of cyclopropylamines with olefins by visible-light photocatalysis. *Angewandte Chemie International Edition* **51,** 222–226 (2012).

22. Lin, Q.-Y., Xu, X.-H. & Qing, F.-L. Chemo-, regio-, and stereoselective trifluoromethylation of styrenes via visible light-driven single-electron transfer (SET) and triplet–triplet energy transfer (TTET) processes. *The Journal of Organic Chemistry* **79,** 10434–10446 (2014).

23. Wei, X.-J., Boon, W., Hessel, V. & Noël, T. Visible-light photocatalytic decarboxylation of α, β-unsaturated carboxylic acids: facile access to stereoselective difluoromethylated styrenes in batch and flow. *ACS catalysis* **7,** 7136–7140 (2017).

24. Welin, E. R., Le, C., Arias-Rotondo, D. M., McCusker, J. K. & MacMillan, D. W. Photosensitized, energy transfer-mediated organometallic catalysis through electronically excited nickel (II). *Science* **355,** 380–385 (2017).

25. Chatterjee, A. & König, B. Birch-Type Photoreduction of Arenes and Heteroarenes by Sensitized Electron Transfer. *Angewandte Chemie International Edition* **58,** 14289–14294 (2019).

26. Coles, M. S., Quach, G., Beves, J. E. & Moore, E. G. A Photophysical Study of Sensitization-Initiated Electron Transfer: Insights into the Mechanism of Photoredox Activity. *Angewandte Chemie* **132,** 9609–9613 (2020).

27. Glaser, F. & Wenger, O. S. Recent progress in the development of transition-metal based photoredox catalysts. *Coordination chemistry reviews* **405,** 213129 (2020).

28. Zhang, M., De Respinis, M. & Frei, H. Time-resolved observations of water oxidation intermediates on a cobalt oxide nanoparticle catalyst. *Nature chemistry* **6,** 362 (2014).

29. Sheng, H. & Frei, H. Direct Observation by Rapid-Scan FT-IR Spectroscopy of Two-Electron-Reduced Intermediate of Tetraaza Catalyst $[Co^{II}N_4H\ (MeCN)]^{2+}$ Converting CO_2 to CO. *Journal of the American Chemical Society* **138,** 9959–9967 (2016).

30. Barrow, G. M. *Introduction to molecular spectroscopy* (McGraw-Hill, 1962).

31. Larkin, P. *Infrared and Raman spectroscopy: principles and spectral interpretation* (Elsevier, 2011).

32. Atkins, P. W. & de Paula, J. *Atkins' physical chemistry* (W. H. Freeman, 2006).

33. Swinehart, D. F. The Beer-Lambert Law. *Journal of Chemical Education* **39,** 333 (1962).

34. Herres, W. & Gronholz, J. Understanding FT-IR data processing, 352–356 (1984).

35. Johnson, T., Simon, A., Weil, J. & Harris, G. Applications of time-resolved step-scan and rapid-scan FT-IR spectroscopy: dynamics from ten seconds to ten nanoseconds. *Applied spectroscopy* **47,** 1376–1381 (1993).

36. Johnson, T. & Zachmann, G. *Introduction to Step-Scan FTIR* (Bruker Optics, 2008).

37. Nakamaru, K. Synthesis, luminescence quantum yields, and lifetimes of trischelated ruthenium (II) mixed-ligand complexes including 3, 3-dimethyl-2, 2-bipyridyl. *Bulletin of the Chemical Society of Japan* **55,** 2697–2705 (1982).

38. Spectra-Physics. *Quanta-Ray Lab-Series Pulsed Nd:YAG Lasers User's Manual* (Author, 2002).

39. Bruker. *VERTEX 70 User Manual* (Author, 2002).

40. Mertz, L. *Transformations in optics* (Wiley, 1965).

41. Forman, M. L., Steel, W. H. & Vanasse, G. A. Correction of asymmetric interferograms obtained in Fourier spectroscopy. *Journal of the Optical Society of America* **56,** 59–63 (1966).

42. Davis, S. P., Abrams, M. C. & Brault, J. W. *Fourier transform spectrometry* (Elsevier, 2001).

43. Hutson, M. S. & Braiman, M. S. Direct phase correction of differential FT-IR spectra. *Applied spectroscopy* **52,** 974–984 (1998).

44. Juris, A, Balzani, V, Barigelletti, F, Campagna, S, Belser, P. l. & von Zelewsky, A. v. Ru (II) polypyridine complexes: photophysics, photochemistry, eletrochemistry, and chemiluminescence. *Coordination Chemistry Reviews* **84,** 85–277 (1988).

45. Kalyanasundaram, K. *Photochemistry of polypyridine and porphyrin complexes* (Academic Press, 1991).

46. Omberg, K. M., Schoonover, J. R., Treadway, J. A., Leasure, R. M., Dyer, R. B. & Meyer, T. J. Mid-infrared spectrum of $[Ru(bpy)_3]^{2+}$. *Journal of the American Chemical Society* **119,** 7013–7018 (1997).